

Wet mono-sized granular packing: effects of initial clusters and filling strategy

Mingrui Dong^a, Zhongzheng Wang^b, Yixiang Gan^{a,c,*}

^a School of Civil Engineering, The University of Sydney, NSW 2006, Australia

^b School of Mechanical, Medical and Process Engineering, Faculty of Engineering, Queensland University of Technology, QLD 4001, Australia

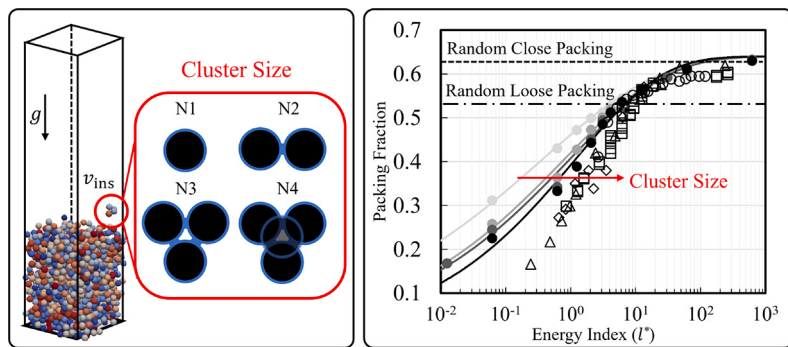
^c The University of Sydney Nano Institute, The University of Sydney, NSW 2006, Australia



HIGHLIGHTS

GRAPHICAL ABSTRACT

- The discrete element method (DEM) is adopted for wet granular packing.
- A packing strategy is applied to control the system with desired packing factor.
- Cohesion effects on packing processes and final morphological structures are shown.
- A dimensionless index is effective to characterise wet granular packing features.



ARTICLE INFO

Keywords:

Mono-sized granular packing
Cohesion
Capillary force
Packing structure

ABSTRACT

Cohesive particles have been demonstrated to affect packing structures that sometimes inhibit applications while helpful in others. Therefore, accurately tailoring the cohesive granular packing, e.g., wet particles, is very rewarding nowadays. We adopt the discrete element method (DEM) and present a packing strategy by falling different size clusters containing mono-sized particles with varying cohesion to tailor the packing structure. We demonstrate the strategy's effectiveness by comparing the result with previous experiments, and we found the larger cluster tends to form a looser packing. We evidence that a dimensionless number, I^* , evaluating the competing importance between kinetic energy and capillary potential, can precisely describe the cohesion effect. We combine I^* with several key indices, e.g., packing fraction, granular temperature, coordination number and force network distribution, to describe packing formation. Meantime, we found the different characterisation of cohesion effect throughout packing stages, which can shed light on the understanding of wet granular packing.

1. Introduction

Granular packing has wide applications and is of fundamental

importance in various disciplines [1]. The packing fraction ϕ (the ratio between solid volume and total volume) is a key index for predicting various properties of granular media [2–4]. For granular packing of

* Corresponding author at: School of Civil Engineering, The University of Sydney, NSW 2006, Australia.
E-mail address: yixiang.gan@sydney.edu.au (Y. Gan).

cohesionless and mono-sized spherical particles in 3D, it has been demonstrated that $\phi \in [0.55, 0.64]$ can be tuned by the friction coefficient [1,5]. $\phi = 0.55$ is widely accepted to represent the lower boundary of stable packing structure that can be constructed, and it is conventionally termed as random loose packing (RLP), while 0.64 corresponds to the random close packing (RCP) structure beyond which ordered structure and crystallization ($0.64 < \phi < 0.74$) may appear to be dominant [6]. Some essential granular properties that can affect packing fraction are particle surface roughness [4], shape [7,8] and size distribution [9]. For very fine and dry particles (the diameter $d < 100 \mu\text{m}$), van der Waal's force can bring cohesion to further decrease the packing fraction to random very loose packing (RVLP) characterising $\phi < 0.55$ [10–12]. Wet granular materials also possess a cohesion effect through introducing pore-scale attractive capillary forces F_n^{cap} [13,14], where n indicates the normal effect. It was reported that F_n^{cap} results from the liquid can dominate granular properties with certain water content [15–17]. When water content rises from zero, liquid bridges can be formed to connect pairs of neighbouring particles and create an increasing F_n^{cap} . For an intermediate water content, the liquid in pores can gradually evolve to liquid patches and F_n^{cap} remains constant. A further increase of water content can diminish F_n^{cap} due to the loss of interfacial area and capillary pressure [13,15,17,18]. Various phenomena such as evaporation and porosity evolution can also characterise the notable impact of pore-scale force on particle contacts [19–21].

Besides particle properties, packing strategy also affects packing formation. Soil pluviation is designed to prepare different soil samples with different densities for soil tests. Tapping [2] and vibration [9,22] with a proper intensity have been verified effective to densify granular structure. Shear and compression are widely used to investigate packing formation in the jammed state [23,24]. For wet particles, Researchers have been using various mechanical strategies to characterise the impact of cohesion. Feng and Yu [19] conducted experiments by slowly pouring wet particles to form the granular packing and found the particle size and surface tension are key controlling parameters to achieve different ϕ . Yang et al. [13] and Parteli et al. [10] both applied the DEM to simulate the pouring strategy by pre-setting cohesive particle assemblies with non-overlap positions and an initial low ϕ to form RVLP. Dong et al. [25] settled particles immersed in liquids with different ratios of inter-particle force to the gravitational force, further investigated the packing process considering the cohesion effect in low gravity conditions. Pacheco-Vázquez et al. [16] poured particles in a tank to observe the granular heap, pile and tower formation with different water content. Moreover, the summarised transition from the heap (dry) to towers (liquid content increase) and further to an underwater pile (particles fully immersed in liquid) correspond well to the results of particle level observation for liquid patch formation using X-Ray [15]. Liu et al. [11] and Wang et al. [14] implemented simulation and experiment separately with controlled falling height of cohesive particles to achieve the target ϕ . Overall, the dimensionless number, which considers the ratio between body force and capillary force, although in different formats, is the common way to investigate the cohesive packing [13,14,25,26]. However, the impact of initial conditions, i.e., preexisting particle clusters, was always neglected.

Researchers have proposed indices to characterise the features of packing formation, such as granular temperature T_g , coordination number Z and force network. The local ϕ and particle moving speed can be used to classify the granular media as gas (particles bouncing quickly), fluid (particles move like fluid flow) and solid (particles can barely move) phases [1,27]. These three phases can coexist at the microstructural scale during typical granular packing processes and evolve over time. A quantified phase transition criterion is proposed to characterise packing processes through the ϕ - T_g relation [1,27–30]. In wet granular cases, the cohesion can change the packing formation process, and a possible shifted T_g - ϕ relation can be obtained [31]. A smooth transition of T_g at the boundary between the fluid and solid is also captured in the rotation drum experiments [30]. For the solid phase,

the morphological structure is significant in applications regarding the liquid movement in pores [21,32], electrical and thermal conductivity through inter-particle contact [33–35], powder bed density in 3D printing technology [12] and manufacturing granulation [36]. The granular morphological structures can be characterised by the coordination number (Z) reflecting the averaged neighbouring quantity of each particle. In the packing fraction range between ϕ_{RLP} and ϕ_{RCP} , Z can vary from around four to around six [4,5], which explains the necessary inter-particle contacts that the packing structure needs to reach a force balanced state [5]. With the help of attractive force in cohesive cases, since the granular force network can have a combined effect of F_n^{cap} and solid contact F_n^{solid} , it can be easier to reach the force balanced state with smaller Z and looser packing structures (smaller ϕ) [18]. Furthermore, an extremely cohesive packing condition with a ϕ_{RVLP} was also reported possessing a chain-like structure [13,26], which evidences the reason for a further reduction of Z to around two. Notably, Z only provides a general structure information to describe the solid phase (the regime of force balanced state), and it cannot fully explain the reason of the structure formation. Therefore, anisotropic force network distribution can help further explain how the structure is formed through contact index Z [7,37]. In a granular heap, the force networks that tend to align along the gravity direction dominate the construction of the packing, leading to an anisotropic packing structure [37]. Although cohesive granular packing has been extensively investigated in recent decades, the effect of cohesion on contact force network is yet fully understood. Several indices considering the angular distribution of contact forces have been proposed and applied to quantify the description of anisotropy [7,38,39]. The force network distribution in cohesive granular packing can be analysed by $F_n^{\text{total}} = F_n^{\text{solid}} - F_n^{\text{cap}}$ [40]. Overall, the anisotropy effect can become obvious under certain directional load [41,42].

In this study, we apply DEM to simulate the packing process of wet mono-sized spheres. We adopt a packing strategy controlling the filling clusters size and the falling height, which are similar to our previous experiments [14]. We set liquid bridges initially connecting the particles in each cluster and investigate the effect of a varying F_n^{cap} . We then validate the effectiveness of this packing strategy by observing ϕ and a dimensionless energy ratio l^* to compare with experiments and simulations from literature. This study can fill the gap that initial conditions for the packing process were not taken into account. We introduce the fundamental governing equation and the model setup in Section 2. Section 3 will start by describing the cohesion effect in the packing process, followed by reporting and discussing the results of the proposed packing strategy and the formed packing morphological structure using means of indices, i.e., ϕ , T_g , Z and force network. Finally, the conclusions are made in Section 4.

2. Method

2.1. Inter-particle force

The DEM was firstly proposed by Cundall and Strack [43] to simulate the particle as the mass point with a prescribed radius for detecting inter-particle contact force. Through the computation of Newton's second law of motion, the movement of each particle is described. With the development of DEM in recent decades [43–45], it has been proven effective in providing particle level information that facilitates the study on granular materials. Here, we apply the DEM established in the open-source platform LIGGGHTS [46]. The normal, tangential and rolling inter-particle contact laws are shown as [47–49]:

$$\begin{aligned} F_n^{\text{solid}} &= k_n \delta_n - \beta_n \nu_n \\ F_t &= k_t \delta_t - \beta_t \nu_t \\ M_r &= k_r \Delta \theta_r - \beta_r \omega , \end{aligned} \quad (1)$$

where n , t and r indicate the normal, tangential and rolling effect,

superscript "solid" indicates the traditional Hertzian contact, F is the contact force, k is the contact stiffness, M is the rolling torque, δ is the overlap distance of each pair of contacting particles, $\Delta\theta_r$ is the relative rotation angle of contacting particles, β is the damping coefficient, v and ω is the relative translational velocity and relative angular velocity for each contact pair, respectively. Here, the tangential friction and rolling effect, F_t and M_r , applies the Coulomb style criteria giving $|F_t| \leq \mu_s |F_n^{\text{total}}|$ and $|M_r| \leq \mu_r R F_n^{\text{total}}$ where μ_s is the sliding friction coefficient and μ_r is the rolling friction coefficient [48], R is the radius of particles. Since μ_s for glass sphere particles can range from nearly 0 to 0.65 [10,13,50–52], a value of $\mu_s = 0.5$ is selected in this study [10,13]. We adopted the restitution coefficient $e = 0.9$ the same as the previous study by Bhateja et al. [52]. To ensure computational stability and physically meaningful [24,43], the integration time step is set using $t = 10^{-8}s < \sqrt{m/Ed_s}$, where m is the mass of the smallest particle, E is the Young's modulus and $d_s = 0.95d$ is the diameter of the smallest particles. Table 1 shows the key parameters adopted.

When the water content is low within the wet granular assemblies, i.e. $m_w \leq 5\%$, the liquid bridge starts dominating the liquid appearance format and providing attractive inter-particle force [15]. Therefore, we consider the primary source of cohesion effect as the capillary force supplied by the liquid bridge. The governing law of capillary force as proposed by Soulie et al. [53] can be expressed as follow:

$$F_n^{\text{cap}} = \pi\gamma\sqrt{R_i R_j} \left[c + e^{(aD/R_j+b)} \right], \quad (2)$$

where F_n^{cap} is the attractive capillary force, γ is the surface tension, R_i and R_j are radius of two liquid bridge connected particles, and j indicate the larger one, D_{gap} is the inter-particle surface gap distance (illustrated in Fig. 1(b)), a , b and c are deduced coefficients from the liquid bridge volume (V_{ij}^{bri}), multi-phase contact angle θ and R_j [53]. Here, we assume the liquid film fully covers surfaces of particles, i.e., $\theta = 0$ [54]. The volume of liquid on each particle is simplified as $V_i^l = V_i \times 5\%$, where V_i is the volume of particle i . To ensure the overall morphology of liquid bridges lie in pendular state [14,15,19], the liquid bridge volume V_i^{bri} is assumed to be $0.05 \times (V_i^l + V_j^l) = (V_i + V_j) \times 0.25\%$. This setting assumes a maximum of 60% of effective volumetric liquid content of one particle (V_i^l) forms liquid bridges when a possible max contact neighbours reach twelve (FCC topological structure). Since the mass ratio between liquid and solid particles is $\rho_l \times \frac{0.05}{\rho_p} \approx 2\%$, the effect of liquid weight on granular packing is negligible. When particles move against each other, a liquid bridge birth distance $D_{\text{birth}} = 0.016(d_i + d_j)$ (shown in Fig. 1(c)) is set to consider the formation of the liquid bridge due to the liquid film thickness h_t . In practice, liquid film thickness on the sphere particle surface is affected by the thermal condition, dynamic perturbation and total liquid volume. When $h_t \ll R$, the difference of thickness on the whole spherical surface can be six orders of magnitude smaller than the particle size [55]. Therefore, in this study, given the 5% volumetric liquid content, the liquid film thickness $h_t = 0.5d \times (1.05^{\frac{1}{3}} - 1) = d \times$

0.82% is assumed to be uniformly distributed, and the dynamic perturbation will be assumed negligible. A threshold for liquid bridge rupture distance $D_{\text{rupture}} = (1 + 0.5\theta) \times (V_{ij}^{\text{bri}})^{\frac{1}{3}}$ [56] is adopted, beyond which the liquid bridge ruptures and F_n^{cap} disappear. A full process of liquid bridge formation and rupture considering different γ is illustrated in Fig. 1 from the state (b) to (d).

Table 1 includes a range of surface tension values, which will be used later to cover the range of parametric space. This has been checked with the scaling analysis.

2.2. Packing strategy

The simulation domain is a rectangular box with periodic boundaries in the x-axis and y-axis (horizontally), and a solid plate is positioned at the bottom (see Fig. 2). The width and length are ten times that of the particle diameter d aiming to meet the need of representative volume element (RVE) [10,13], eliminate the wall effect [22] and keep the simulation efficient. Thus, this setting can be seen as a part extraction of the physical experiment by Wang et al. [14].

To simulate the falling process with a constant height h_{fall} , particles are inserted one by one or cluster by cluster at the position with distance d higher than that of the existing particles that possess the maximum z (vertical position). The insertion position in the x-y plane is randomly distributed within the x-y cross-section, so as the total height of the packing structure increases, the insertion position along the z-axis will follow up. A velocity, v_{ins} , is applied to inserted particle clusters to model an constant falling height h_{fall} , and it is obtained by $v_{\text{ins}} = \sqrt{2gh_{\text{fall}}}$. In comparison, the constant v_{ins} scenario is not considered both in the experiment [14] and simulations [10,11,13,57], where h_{fall} can be decreased due to the the fixed initial particle filling position and a rise of H , and this can be crucial in practical engineering problem [58,59] as $v_{\text{ins}} = \sqrt{2g(h_{\text{fall}} - H)}$. Here, our constant h_{fall} can ensure a constant effective falling height to prevent the impact of a decreasing h_{fall} and, consequently, form a consistent ϕ along the depth, i.e., the z direction. In all cases, particle size are uniformly distributed with $d \pm 5\%$ to avoid crystallization [22,60].

With the given range of γ and μ_v , since the maximum velocity in our simulation $v_{\text{max}} \propto v_{\text{ins}}$, the capillary number $C_a = \frac{v_{\text{max}}\mu_v}{\gamma\cos(\theta)} \ll 1$ indicates the viscosity effect can be negligible in this study. The dimensionless number evaluating the importance of kinetic energy and capillary potential are used to characterise the cohesion effect [14] as:

$$l^* = \frac{E_k}{E_{\text{cap}}} , \quad (3)$$

where $E_k = \frac{1}{2}mv_{\text{ins}}^2 = mgh_{\text{fall}}$ considers the initial kinetic energy converted from the gravitational potential due to a constant falling height, and $E_{\text{cap}} = 2\pi\gamma R \cos(\theta)d$ considers the capillary potential. In our simulations, the surface tension γ is varied (see Table 1) to tune the relative extent of cohesion. Though these values may exceed the range of the physical system, the sole purpose of varying l^* , which can be achieved equivalently by combining other parameters in Eq. (3), e.g., the particle size. This dimensionless number can be interpreted as a competition of the impact energy versus dissipation capacity of the porous media when receiving the perturbation, which means either smaller E_k or greater E_{cap} can lead to a decrease of l^* , implying less compaction and thus a looser packing state. We will further discuss the validity of using l^* to characterise packing formation in Section 3.

Particles are generated sequentially to form an initial cluster. Taking N4 as an example, the first particle is generated with a random position in x-y plane and a certain vertical position z , other particles are then generated based on the position of the first particle while keeping the centre distance equal to D_{birth} among each other. This setup facilitates the liquid bridge to pre-exist (see D_{birth} in Fig. 1(c)). The inset (a) in

Table 1
Model parameters.

Parameter	Value
Young's modulus, E (Pa)	6×10^{10}
Coefficient of sliding friction, μ_s (-)	0.5
Coefficient of rolling friction, μ_r (-)	0.01
Coefficient of restitution (-)	0.9
Surface tension, γ (N/m)	[0.00073, 7.3]
Contact angle, θ (rad)	0
Gravitational acceleration, g (m/s ²)	9.81
Liquid dynamic viscosity, μ_v (Pa · s)	8.9×10^{-4}
Particle diameter, d (μm)	$560 \pm 5\%$
Particle density, ρ (kg/m ³)	2460
Falling height, h_{fall} (mm)	100
Container length\width, LW (-)	$10d \times 10d$
Volumetric liquid content, V_l/V_{solid} (-)	5%

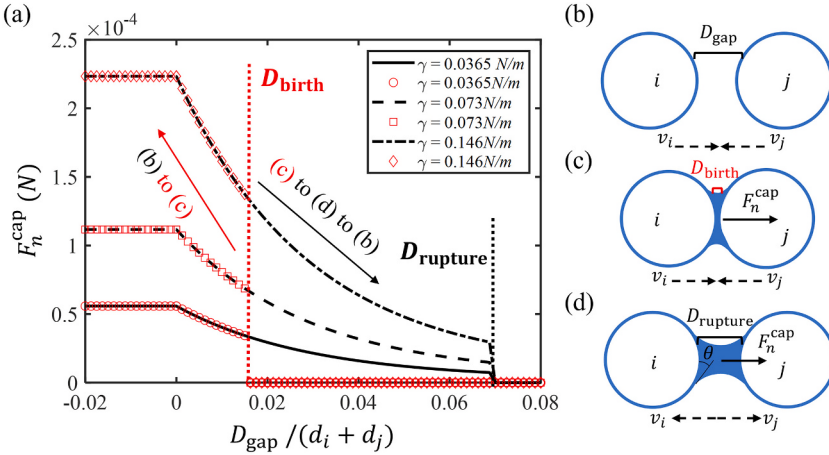


Fig. 1. The capillary force F_n^{cap} model. (a) The line chart shows the smooth transition between state in subplot (b)-(d) governed by Eq. (2) with three values of surface tension γ . Red markers indicate the liquid bridge birth process when $D_{\text{gap}} \leq D_{\text{birth}}$. Black lines indicate the liquid bridge rupture process when $D_{\text{gap}} \geq D_{\text{rupture}}$. (b)-(d) visualise three states of F_n^{cap} as no liquid bridge exist (b), liquid bridge formation due to $D_{\text{gap}} \leq D_{\text{birth}}$ (c), and liquid bridge close to rupture when $D_{\text{gap}} \leq D_{\text{rupture}}$ respectively (d). Here, θ indicate the multi-phase contact angle. (For interpretation of the references to colour in this figure legend, the reader is referred to the web version of this article.)

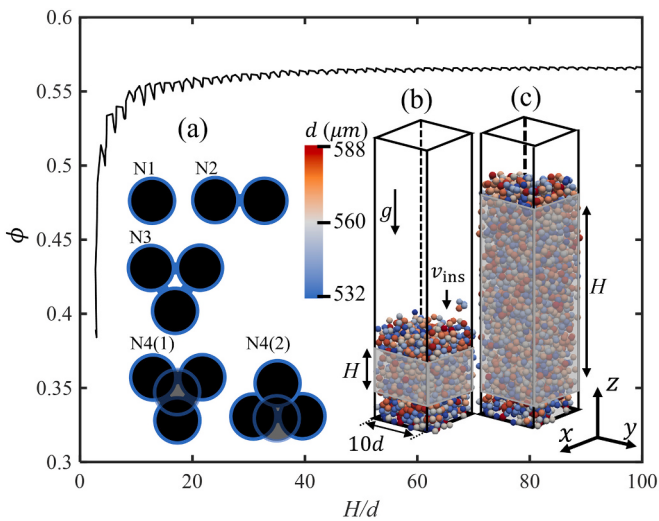


Fig. 2. Evolution of packing fraction ϕ with respect of normalized sample height H/d during the packing formation process, and insets illustrate the model setup. Inset (a) visualises inserted clusters, and $N1-N4$ represents the particle numbers in the clusters. To be noted, since the randomness is set for each inserted cluster, the structure against the direction of gravity g is also random, e.g., possible structure arrangements $N4(1)$ and $N4(2)$. Insets (b) and (c) visualise the simulation domain, and particles colour represents the overall uniformly distributed particle size by $560 \mu\text{m} \pm 5\%$. v_{ins} is the initial velocity of particles as they are generated. H indicate the sampling region of the pile aiming to eliminate the boundary effect ($5d$) and to calculate ϕ .

Fig. 2 illustrates clusters ($N1-N4$) studied in this paper. The line plot in Fig. 2 shows an example describing the overall packing process by the $\phi - \frac{H}{d}$ relation, where H is the sampling region (see the shaded area in Fig. 2(b) and (c)). This sampling window H aims to avoid the boundary region particles by $5d$ for top and bottom packing surfaces. As the packing process continues, ϕ increases with $\frac{H}{d}$ until reaching an asymptotic line at $\frac{H}{d} \approx 30$ where the packing structure is assumed to remain constant.

3. Results and discussion

3.1. Packing formation

The packing formation can be described by the jamming transition of particles from a gas or fluid state to a solid state [1,27]. Particles are free to move in the gas or fluid state, so they are under the force in-

equilibrium state. In the solid state, i.e., the jammed state, particle movement are restrained by contacting neighbours (the force equilibrium state), and an extra external load can lead to a compression or shear stress build-up. Quantitatively, the jamming transition can be further explained by the granular temperature T_g [1,27,30]. One typical definition of granular temperature describing the intense of particles movement is proposed as:

$$T_g = \frac{1}{2N_t} \sum_i^{N_t} m_i (v_i - v_{\text{ave}})^2 , \quad (4)$$

where m_i is the particle mass, v_i is the particle velocity, v_{ave} is the average velocity in the target (sampling) region, the operator \sum integrate all particles in the sampling region and N_t is the total number of particles in that region [1,30].

As shown in Fig. 3(a), the velocity colour profile along the vertical axis shows that velocity decreases from the upper surface downwards since newly inserted particles impact the top region. The value of $l^* = 617, 12.3$ and 3.09 are taking as examples to show the increase trend of the cohesion effect and no specific criterion for the selection of them is applied. The dash line for distinguishing gas, fluid and jammed phase are only for guide of eye to help explain the concept of phase transition which will be characterised in Fig. 3 (b) and (c). The relation between granular movement intensity and granular structure formation can be quantified using T_g and ϕ , which is illustrated in Fig. 3(b), where red lines represent T_g and blue lines represent ϕ . Here, the sampling window (target region) depth of T_g (Eq. (4)) and ϕ is set as $5d$ as the minimum REV size. When tuning the particle to be less cohesive relative to the kinetic energy ($l^* = 617$), T_g decreases more significantly as the transition from fluid to solid than that of relatively high cohesive conditions, i.e., $l^* = 3.09$. This phenomenon can be explained as that when particles are more cohesive, the energy can transmit deeper (downwards of z axis) of the pile, which leads to the raise of T_g within the domain of ϕ_c (showed in Fig. 3(b)), while with less cohesive cases the energy can dissipate within the shallow layer of the packing through frequent bounce back collisions. Note the sampling period of these snapshots is after the asymptotic line is reached (showed in Fig. 2), thus, although the residual fluctuation of DEM particles exists, it has negligible influence on the final formed structures in the jammed phase. Therefore, the T_g caused by the residual fluctuation does not affect the observation of phase transition. To capture the evolution processes of the packing formation, we plot the $\Delta\phi = \phi - \phi_c$ versus T_g for over a hundred snapshots of the plot in Fig. 3 (b) during the packing process along with the increase period of H , and finally combine a smoothing probability density function [61] to form Fig. 3 (c) (Please refer to the Fig. S1 in the supplementary materials for the detail of the probability density plots). In Fig. 3(c), smoothed probability density plots indicate the distribution of the $T_g - \Delta\phi$ lines, and

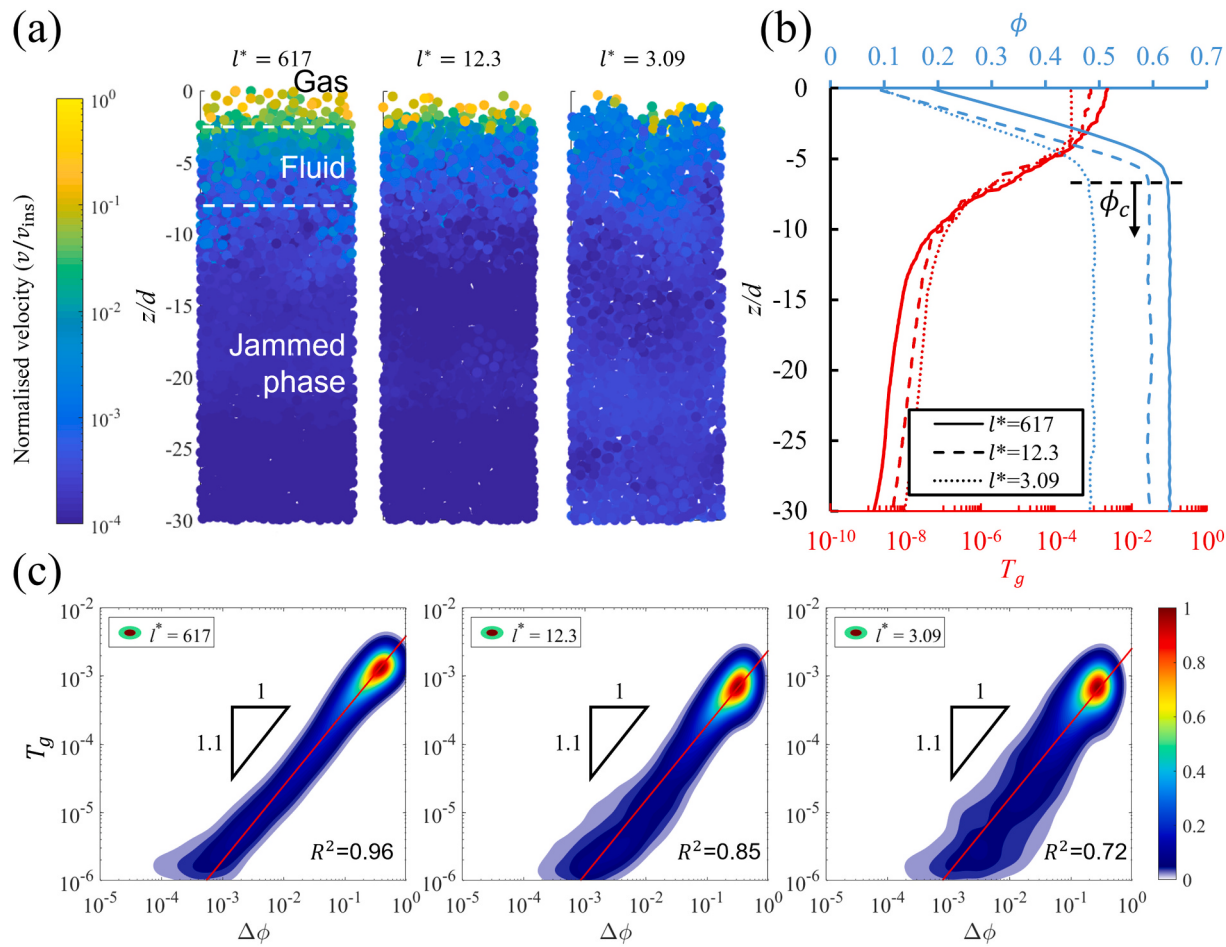


Fig. 3. Phase transition during packing processes as evaluated by granular temperature T_g and packing fraction ϕ . (a): The contour plot illustrates normalized velocity with energy ratio $l^* = \{617, 12.3, 3.09\}$. The gas, fluid and solid zone [1] are annotated corresponding to the velocity profile. (b): T_g and ϕ profiles along with the vertical direction corresponding to the subplot (a). (c): The normalized probability density plot of the relation between T_g and $\Delta\phi$ for cases corresponding to the subplot (a), and the colour transition indicate the normalized probability density $\text{PDF} \in [0, 1]$ (please refer to the supplementary material for the detail). The result is obtained with more than a hundred of the subplot (b) during the packing process with a specific interval of $\delta H/d$, where $\Delta\phi = \phi - \phi_c$, and ϕ_c is ϕ in the region that granular structure is jammed and unchanged corresponding to the region below horizontal black dash line in subplot (b). The red fitting lines possess the same slopes of 1.1 with lower goodness of fitting when cohesion increases (l^* decreases). (For interpretation of the references to colour in this figure legend, the reader is referred to the web version of this article.)

the red area indicates where most lines will pass through, while light blue means T_g - $\Delta\phi$ lines sparsely distribute. Red trend lines indicate fittings of density plots using function $T_g = b\Delta\phi^a$ [29], where the power $a = 1.1$ is consistent (illustrated by triangles in Fig. 3(c)), and $b = 3.9 \times 10^{-3}$, 2.4×10^{-3} , 2.6×10^{-3} with the goodness of fitting $R^2 = 0.96$, 0.85 , 0.72 corresponding to cohesion cases $l^* = 617$, 12.3 , 3.09 , respectively. For a less cohesive case ($l^* = 617$), a converged $\Delta\phi$ - T_g relation with $R^2 = 0.96$ indicates the certainty of settling process will follow the power $a = 1.1$ trend, while the more cohesive case ($l^* = 3.09$) shows a divergence of $\Delta\phi$ - l^* relation with $R^2 = 0.72$ explaining the cohesion is dominant and can lead to uncertainty for the packing formation. On the one hand, this uncertainty and a wider range of the density distribution indicate that the range of T_g for inserted particles to be settled in the solid regime can be wider due to the capillary forces, F_n^{cap} . On the other hand, the slope of 1.1 and divergence can be a combination of the damping effect (coefficient of restitution) and F_n^{cap} , which is worth further investigation. Therefore, the major characterisation of cohesion during the packing formation is the divergence of $\Delta\phi$ - T_g relation, which shows that a strict gas, fluid or solid region becomes harder to define in more cohesive cases.

3.2. Effects of cluster filling strategy

We first observe the global granular structure index packing fraction ϕ . Fig. 4 shows ϕ as a function of l^* for simulations with different initial cluster sizes. The index ϕ presents a monotonic uptrend when the cohesion effect gradually reduces (increasing l^*). At low cohesion, i.e., $l^* > 10$, a collapse of data are observed with $\phi_{\text{RLP}} < \phi < \phi_{\text{RCP}}$, regardless of initial cluster size. At high cohesion, i.e., smaller l^* , however, under the same l^* , smaller ϕ is associated with decreasing cluster size.

A cluster can be assumed as a coarse-grained particle with a certain shape, [62], and ϕ of thus particles can be affected comparing with the spherical particles [8,63]. Therefore, the packing problem due to coarse-grained clusters can be explained by whether the cluster will break (split) or not during the packing process, which will be further discussed in the next paragraph. The data from previous experiments and numerical studies are plotted in Fig. 4 for comparison. In our previous study [14], the falling particles can appear as small clusters due to the sieve mesh size (2–3 times the size of particles), leading to the trend matching well in our studies, whilst the discrepancy will be further discussed below. A decreasing falling height, i.e., $h_{\text{fall}} - H$, can result in a decreased initial kinetic energy (Eq. (3)) in studies of Wang et al. [14] and Yang et al. [13], which can be the reason for the low ϕ , especially in

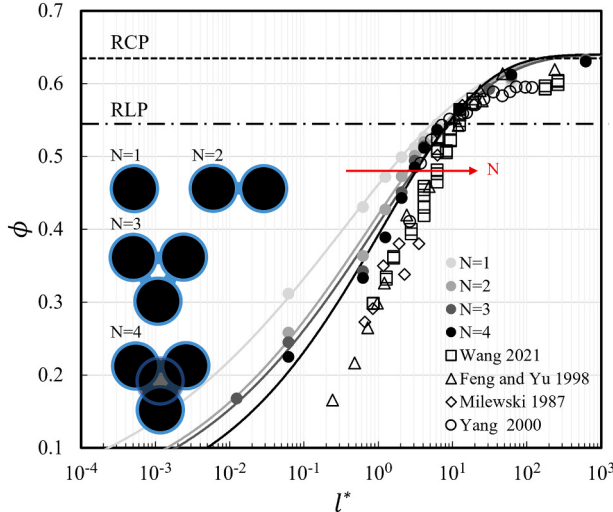


Fig. 4. Packing fraction tuned by the energy ratio index, l^* , and initial falling clusters $N1-N4$. The filled circles are the DEM results of this study. Gray scales from light to dark indicate the transition of four cases from $N1$ to $N4$, and the arrow indicates the direction of increasing N . Solid lines are trend lines of four cases of different cluster sizes. Hollow markers are from literature as a comparison. The predefined initial clusters in different sizes are illustrated through black circles connected by blue liquid bridges. Dotted and dashed horizontal lines denote the packing fractions at random close packing state ($\phi_{RCP} \approx 0.64$) and the lower boundary of random loose packing ($\phi_{RLP} \approx 0.55$), respectively. (For interpretation of the references to colour in this figure legend, the reader is referred to the web version of this article.)

a more cohesive condition. In addition, the wall effect [14] is another reason that ϕ is low when cohesion increases. Compared to experiments by Feng and Yu [19] and Katz and Milewski [64], instead of a cluster falling strategy, a particle pouring approach was adopted. The pouring approach in experiments may not be able to restrain the size of the initial clusters as $N1$. As a result, a similar trend of $\phi-l^*$ relation with that of Wang et al. [14] can be captured. Furthermore, for the simulation by Yang et al. [13], a pouring-like simulation similar to that of Feng and Yu [19] was adopted. Although an initial setup with low ϕ was predefined to avoid the overlap between particles, the bulk falling process (all particles falling simultaneously) can also lead to the cluster formation before or as particles transition from the dynamic regime to static condition. Therefore, we can conclude that the control over the initial condition can help precisely tailor the packing formation. The result helps explain the uncertainty of packing formation when cohesion is hardly avoided and the initial clusters are not controlled, which will be further discussed below.

The particle scale cluster characterisation is analysed through looking at statistics of the cluster breakage. To consider whether particles in clusters will split or remain stick with each other after impacting the top surface of the pile, we define the residual contact, $C_r = N_r/N_t$, to quantify the residual contacts in original clusters, where N_r is the remaining contact in clusters, and N_t is total contacts summed in all initial clusters. Thus, $C_r = 1$ means the falling cluster remains intact (unsplit) due to the F_n^{cap} after the impact, whereas $C_r = 0$ is associated with fully split particle pairs when the falling cluster is less cohesive. Fig. 5 plots the correlation between C_r and l^* . Three zones are classified and illustrated to represent the stick-split state of clusters, i.e., a Stick Zone (STZ) for most clusters remain unsplit, a Stick-Split Zone (SSZ) for most clusters partially split, and a Split Zone (SPZ) for most clusters fully split. As shown in Fig. 5, with the decrease of cohesion (l^* increase), clusters tend to split, while within SSZ, an obvious transition can be observed. Interestingly, the onset of the decrease in C_r , i.e., the suppression of particles separation in clusters upon impact, is associated with $l^* \approx 1$.

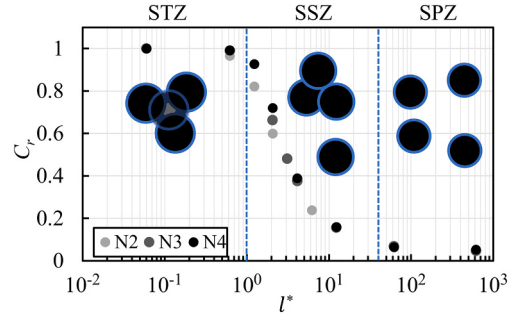


Fig. 5. Residual contact C_r versus energy ratio index l^* . Stick Zone (STZ), i.e., C_r reaches 1, implies particles in most clusters remain unsplit. Stick-Slip Zone (SSZ) represents particles in most partially separated clusters. Split Zone (SPZ) indicates particles in most clusters are split to form new contacts.

3.3. Topological analysis

The mean coordination number (Z_m) is a critical index in studies of granular topological structure [4,5,13], and it describes the number of neighbours for each particle. To illustrate the cohesive cluster effect, here we obtain Z_m by setting a critical particle centre distance equal to D_{birth} , which is a similar setting to Yang et al. [13], and the relation between Z_m versus ϕ is plotted in Fig. 6 (a). In Fig. 6 (a), the solid line maps a triangle area where the mean coordination number Z_m falls between four and six [5] for dry packing conditions. Within the triangle, the broader range of Z_m follows the increase of ϕ depending on different friction coefficient cases. The maximum Z_m for each friction coefficient case forms the upper slope of the triangle [5]. As a comparison for wet cohesive packing conditions, we report similar trends with Yang et al. [13] that Z_m increases monotonically with ϕ , and a collapse of data are observed regardless of N for $\phi > 0.45$. For $\phi \leq 0.45$, the cluster size starts to affect the $Z_m-\phi$ relation. As a comparison, Yang et al. [13] considered the initial packing structure as non-contacting conditions before particles falling. In our cases, $N1$, represented by the lightest gray circles, have a closer trend with the cross than larger initial cluster cases (see Fig. 6 (a)). In Fig. 6 (b)-(e), the distribution of coordination number Z for all particles in $N1-N4$ are shown. Since the cluster effect dominate when cohesion is high, higher probabilities of Z_m can be found in larger cluster cases such as $N3$ and $N4$. As the cohesion decrease, the distribution of all cases shift towards the higher coordination number, i.e., peak at $Z \approx 6$, corresponding to the increase trends in Fig. 6 (a).

Since most clusters tend to remain unsplit with greater cohesion effects (see STZ and SSZ in Fig. 5), the final Z_m of greater cluster size case, i.e., $N4$, tends to be kept larger than the small cluster, i.e., $N2$. During the packing formation, the mean coordination number formed by new contacts can be decomposed and classified as Z_{pp} (inter-particle), Z_{cp} (cluster-particle) and Z_{cc} (inter-cluster), as illustrated in the Fig. 7 (b). Whilst the residual contacts, Z_{old} , from the original clusters can be counted as Z_{ic} (intra-cluster). Across the cluster sizes, the new contacts can play an important role as the cohesion decreases, which results in a higher Z_m . The trends of “old” and “new” contacts at the final stage can be demonstrated in Fig. 7 (a). When the relative cohesion is high (STZ), Z_m is mainly dominated by the Z_{old} for $N3$ and $N4$. As the cohesion decreases (SSZ), the residual contacts gradually play less roles on forming Z_m , which can be observed through the increase of Z_{new} and the decrease of Z_{old} . When the cohesion is considerably low (SPZ), the cluster size effects become negligible. Overall, it can be concluded that the small relative cohesion (i.e., large l^*) eliminates the effect of the initial cluster sizes.

To investigate the packed granular structure, the contact force distribution is determined from the DEM simulation. The contact force anisotropy can arise under different external loads, e.g., gravity, shear, axial and biaxial compression [7,37,38,65]. To elucidate the effect of cohesion on granular contact force anisotropy, we plot the normal force

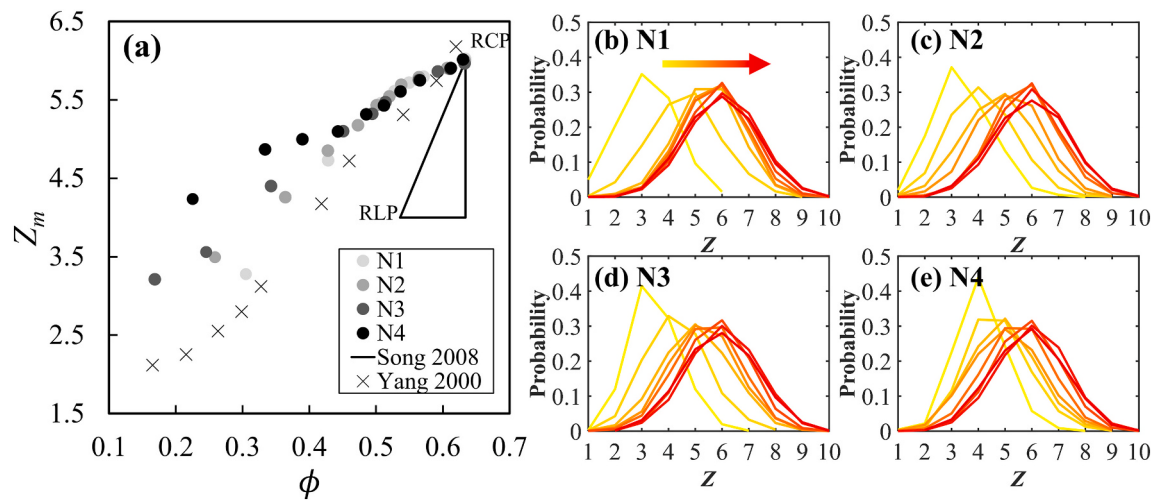


Fig. 6. Cluster effects on Mean coordination number Z_m and coordination number probability distribution. (a): Mean coordination number Z_m vs packing fraction ϕ . Filled circles indicate N1-N4 cases from light gray to black. The cross is from the literature by Yang et al. [13] with a pouring packing strategy. The triangle predicts the possible ϕ_{RLP} and ϕ_{RCP} for dry particles with different friction coefficients [5]. (b)-(e): Coordination number distribution of all particles for cases N1-N4. The colour transition from yellow to red represents the decrease of cohesion effects. (For interpretation of the references to colour in this figure legend, the reader is referred to the web version of this article.)

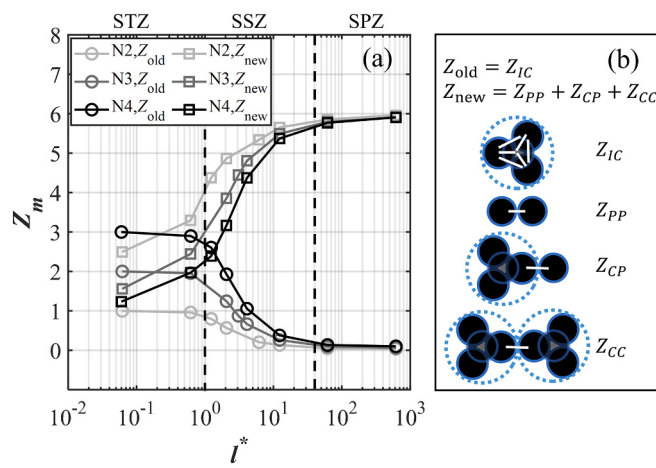


Fig. 7. The analysis of decomposed mean coordination number. (a): The mean coordination number of Z_{old} (residual contacts from original clusters) and Z_{new} as the function of l^* . The vertical dash lines mark the same zones classified in the Fig. 5. (b) The illustrations of decomposed coordination numbers as intra-cluster, inter-particle, cluster-particle and inter-cluster, Z_{IC} , Z_{PP} , Z_{CP} and Z_{CC} , respectively, with contacts indicated by white segments.

F_n (case N4) against the angle α , where α is the angle between the F_n vector and the horizontal direction (x-y plane). Here, $\alpha \pm 7.5^\circ$ is the sampling window size with moving steps range in $[0^\circ 90^\circ]$ (see the inset in Fig. 8(a)). Note, the selection of the angle $\pm 7.5^\circ$ is a trade-off method. Below $\pm 7.5^\circ$, the averaged contact direction results can have large statistical fluctuation. A larger value can hide the anisotropy phenomena. The normal forces F_n^{cap} , F_n^{solid} and F_n^{total} are plotted as shown in Fig. 8(a)-(c). The force anisotropy increases with l^* and ϕ for all three F_n cases when force distribution lines transition from a circle-like shape to ellipsoids [7]. It can be deduced that when the l^* and ϕ is dramatically small, the packing structure possesses a random chain-like structure [13] in all directions, and in this case, F_n^{cap} can dominate packing structure leading F_n^{solid} and F_n^{total} to be close to a circle shape showed in Fig. 8(b) and (c). As a comparison, the case N1 is shown as Fig. S2 in the supplementary materials. It can be concluded that the cluster size has little effect on the isotropic granular fabric formation when cohesion is high. The reason is that the insertion strategy (the horizontal position

and the contact orientation that is led by the intra-cluster particle arrangement) of each cluster of the packing formation is random, and this randomness is retained by the strong capillary force during packing formation. Therefore, the cluster effects can only be reflected in the statistical analysis of coordination number Z_m . The strong cohesion results in more stable granular skeleton, which is reflected by smaller coordination number (Fig. 6). So, the isotropy and Z_m of the granular skeleton are the result of the competition between cohesion effects and gravitational force. The orientation distribution of the normalized force when gravity dominate ($\phi > 0.55$) is also comparable with the dry condition by Fan et al. [39] (in their work $\phi \approx 0.6$ at relax before compression), where a larger vertical contact force distribution indicating the dominance of the gravity is found. Therefore, As the relative cohesion decreases (l^* increases), the gravitational force becomes dominant with a denser (ϕ increases) packing structure, which lead the force networks (F_n^{solid}) contributing more to the overall packing construction, and the F_n^{solid} tend to align with the direction of gravity. This force anisotropy can explain the cohesion-induced increase of heap height with a larger angle of repose (AOR) [12].

Furthermore, we apply a harmonic style approximation to quantify the force anisotropy, i.e., Eq. (5) proposed by Azéma et al. [7]:

$$\overline{F_n}(\alpha)/\overline{F_n} = 1 + A(3\cos^2(\alpha) - 1), \quad (5)$$

where F_n is the normal force of each contact pair, α is the sampling window size, A is the anisotropy index, the symbol over-line indicate the average operator with $\overline{F_n}$ as the average of the F_n of all contacts in the packing. Here, the index A successfully quantifies the transition of contact force distribution under different cohesion intensity (see the comparison between dots and solid lines in Fig. 8). The index A is then plot against l^* , showed in Fig. 8(d). As can be seen, F_n^{total} and F_n^{solid} start diverge from F_n^{cap} at $l^* \approx 1$, while the F_n^{solid} gradually becomes dominant when F_n^{total} gradually converges to F_n^{solid} as the packing possesses less cohesion (l^* increase).

4. Conclusions

In this work, wet granular packing has been simulated using DEM with consideration of capillary interaction between particles. A packing strategy considering the initial falling cluster size is adopted to precisely tailor the overall packing structure. It is demonstrated that the initial condition can be crucial to the cohesive packing process. The

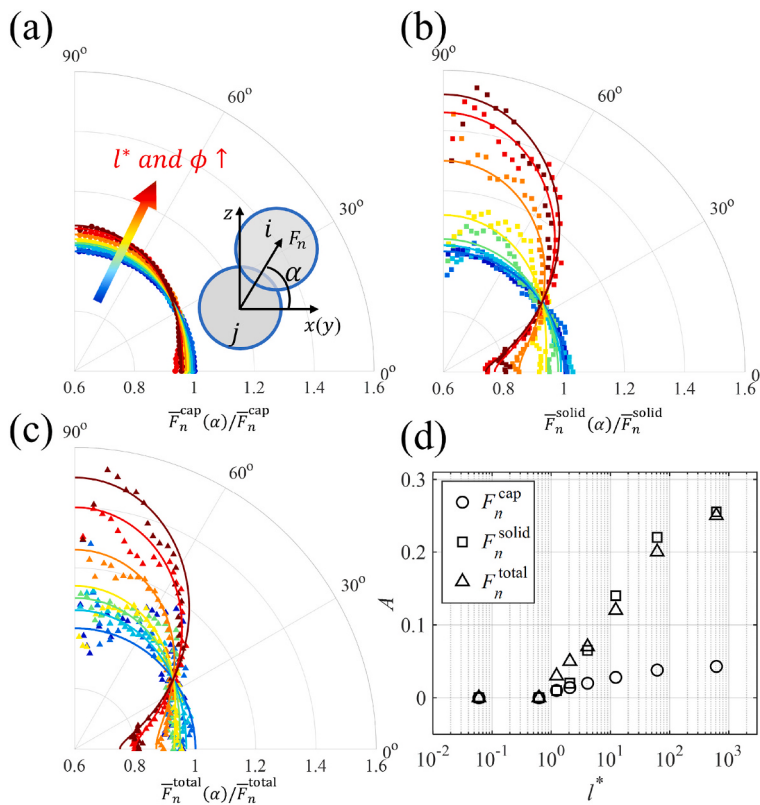


Fig. 8. Anisotropy of normal contact forces. (a)-(c): The polar distribution of normalized capillary force (\bar{F}_n^{cap} with symbol \circ), Hertzian contact (\bar{F}_n^{solid} with symbol \square) and total normal force (\bar{F}_n^{total} with symbol \triangle) respectively. The overline symbol represent the average operator. A “jet” colormap transition from blue to red indicates the decrease of cohesion where l^* rise as $\{0.06, 0.62, 1.23, 2.06, 4.11, 12.3, 61.7, 617\}$ and the corresponding $\phi = \{0.23, 0.33, 0.39, 0.44, 0.51, 0.57, 0.61, 0.63\}$. The force sampling angle α is illustrated by the inset in subplot (a). (d): the anisotropy index A obtained from Eq. (5). (For interpretation of the references to colour in this figure legend, the reader is referred to the web version of this article.)

dimensionless number index (l^*) capturing the relative importance of particle falling kinetic energy and capillary potential is applied to describe the intensity of cohesion. The cohesion effect on the granular packing formation is well characterised by granular temperature T_g , coordination number Z , anisotropy index A , and cluster separation ratio C_r that all are found to be related to l^* and packing fraction ϕ . The main conclusions based on our analyses are:

- The simulation results are compared quantitatively to experimental data sets highlighting the influence of capillary interactions, as well as the initial cluster size.
- A larger initial cluster size under the same cohesion, i.e., same l^* , can lead to a lower packing fraction and a higher coordination number (Z).
- Wet granular packing processes have been described using a power-law relation between $\Delta\phi$ and T_g , and higher uncertainty was captured for relatively high cohesion (for a smaller l^*).
- For relatively high cohesion (for a smaller l^*), a more isotropic force distribution can be obtained, while an anisotropic condition can be observed as the gravitational force becomes dominant (for a larger l^*).

It is worth considering further works: 1) the underlying mechanisms, e.g., different grain-scale dissipation modes, of the observed divergence phenomena of T_g - $\Delta\phi$ relation during wet granular packing formation, 2) the computational model on describing liquid morphology beyond pendular state when liquid content varies. This study presents the particle scale details of wet granular packing with focusing on the role of initial filling cluster size, surface tension and formed topological structure. Conclusions have implications on several industrial applications, e.g., unsaturated soil sample preparation through pluviation, powder bed preparation for laser selective melting in additive manufacture, and pharmaceutical granulation.

CRedit authorship contribution statement

Mingrui Dong: Conceptualization, Methodology, Formal analysis, Visualization, Writing – original draft. **Zhongzheng Wang:** Conceptualization, Formal analysis, Writing – review & editing. **Yixiang Gan:** Conceptualization, Supervision, Writing – review & editing.

Declaration of Competing Interest

The authors declare that they have no known competing financial interests or personal relationships that could have appeared to influence the work reported in this paper.

Appendix A. Supplementary data

Supplementary data to this article can be found online at <https://doi.org/10.1016/j.powtec.2022.117678>.

References

- [1] B. Andreotti, Y. Forterre, O. Pouliquen, *Granular Media: Between Fluid and Solid*, Cambridge University Press, 2013.
- [2] A. Yu, J. Hall, Packing of fine powders subjected to tapping, *Powder Technol.* 78 (1994) 247–256.
- [3] S. Luding, So much for the jamming point, *Nat. Phys.* 12 (2016) 531–532.
- [4] Y. Yuan, Y. Xing, J. Zheng, Z. Li, H. Yuan, S. Zhang, Z. Zeng, C. Xia, H. Tong, W. Kob, et al., Experimental Test on Edwards Volume Ensemble of Tapped Granular Packings, arXiv preprint. [arXiv:2103.07869](https://arxiv.org/abs/2103.07869), 2021.
- [5] C. Song, P. Wang, H.A. Makse, A phase diagram for jammed matter, *Nature* 453 (2008) 629–632.
- [6] A. Baule, F. Morone, H.J. Herrmann, H.A. Makse, Edwards statistical mechanics for jammed granular matter, *Rev. Mod. Phys.* 90 (2018), 015006.
- [7] E. Azéma, F. Radjai, F. Dubois, Packings of irregular polyhedral particles: strength, structure, and effects of angularity, *Phys. Rev. E* 87 (2013), 062203.
- [8] A. Farsi, J. Xiang, J.-P. Latham, M. Carlson, H. Stitt, M. Marigo, Packing simulations of complex-shaped rigid particles using fdem: An application to catalyst pellets, *Powder Technol.* 380 (2021) 443–461.

- [9] S.R. Jaggannagari, R.K. Desu, J. Reimann, Y. Gan, M. Moscardini, R. K. Annabattula, Dem simulations of vibrated sphere packings in slender prismatic containers, *Powder Technol.* 393 (2021) 31–59.
- [10] E.J. Parteli, J. Schmidt, C. Blümel, K.-E. Wirth, W. Peukert, T. Pöschel, Attractive particle interaction forces and packing density of fine glass powders, *Sci. Rep.* 4 (2014) 1–7.
- [11] W. Liu, S. Li, S. Chen, Computer simulation of random loose packings of micro-particles in presence of adhesion and friction, *Powder Technol.* 302 (2016) 414–422.
- [12] M.Y. Shaheen, A.R. Thornton, S. Luding, T. Weinhart, The influence of material and process parameters on powder spreading in additive manufacturing, *Powder Technol.* 383 (2021) 564–583.
- [13] R. Yang, R. Zou, A. Yu, Computer simulation of the packing of fine particles, *Phys. Rev. E* 62 (2000) 3900.
- [14] Z. Wang, J.-M. Pereira, Y. Gan, Packing of wet monodisperse spheres, *Powder Technol.* 378 (2021) 60–64.
- [15] M. Scheel, R. Seemann, M. Brinkmann, M. Di Michiel, A. Sheppard, B. Breidenbach, S. Herminghaus, Morphological clues to wet granular pile stability, *Nat. Mater.* 7 (2008) 189–193.
- [16] F. Pacheco-Vázquez, F. Moreau, N. Vandewalle, S. Dobolo, Sculpting sandcastles grain by grain: self-assembled sand towers, *Phys. Rev. E* 86 (2012), 051303.
- [17] J.N. Israelachvili, *Intermolecular and Surface Forces*, Academic press, 2015.
- [18] S. Herminghaus*, Dynamics of wet granular matter, *Adv. Phys.* 54 (2005) 221–261.
- [19] C. Feng, A. Yu, Effect of liquid addition on the packing of mono-sized coarse spheres, *Powder Technol.* 99 (1998) 22–28.
- [20] B. Mielniczuk, T. Hueckel, M.S. El Youssoufi, Evaporation-induced evolution of the capillary force between two grains, *Granul. Matter* 16 (2014) 815–828.
- [21] Z. Wang, B. Maillet, J.-M. Pereira, Y. Gan, Towards the end of drying of granular materials: enhanced evaporation and drying-induced collapse, *Water Resour. Res.* 57 (2021), e2021WR030125.
- [22] W. Dai, J. Reimann, D. Hanaor, C. Ferrero, Y. Gan, Modes of wall induced granular crystallisation in vibrational packing, *Granul. Matter* 21 (2019) 1–16.
- [23] C.S. O'Hern, S.A. Langer, A.J. Liu, S.R. Nagel, Random packings of frictionless particles, *Phys. Rev. Lett.* 88 (2002), 075507.
- [24] Y. Gan, M. Kamlah, Discrete element modelling of pebble beds: with application to uniaxial compression tests of ceramic breeder pebble beds, *J. Mech. Phys. Solids* 58 (2010) 129–144.
- [25] K. Dong, R. Yang, R. Zou, A. Yu, Role of interparticle forces in the formation of random loose packing, *Phys. Rev. Lett.* 96 (2006), 145505.
- [26] D. Kadau, H.J. Herrmann, Density profiles of loose and collapsed cohesive granular structures generated by ballistic deposition, *Phys. Rev. E* 83 (2011), 031301.
- [27] A.J. Liu, S.R. Nagel, Jamming is not just cool any more, *Nature* 396 (1998) 21–22.
- [28] C.S. O'hern, L.E. Silbert, A.J. Liu, S.R. Nagel, Jamming at zero temperature and zero applied stress: the epitome of disorder, *Phys. Rev. E* 68 (2003), 011306.
- [29] Z. Zhang, N. Xu, D.T. Chen, P. Yunker, A.M. Alsayed, K.B. Aptowicz, P. Habdas, A. J. Liu, S.R. Nagel, A.G. Yodh, Thermal vestige of the zero-temperature jamming transition, *Nature* 459 (2009) 230–233.
- [30] A. Jaray, V. Magnanimo, S. Luding, Wet granular flow control through liquid induced cohesion, *Powder Technol.* 341 (2019) 126–139.
- [31] N. Mitarai, F. Nori, Wet granular materials, *Adv. Phys.* 55 (2006) 1–45.
- [32] Z. Shi, Z. Wang, Y. Gan, Effects of topological disorder in unsaturated granular media via a pore-scale lattice boltzmann investigation, *Adv. Water Resour.* 149 (2021), 103855.
- [33] W. Dai, D. Hanaor, Y. Gan, The effects of packing structure on the effective thermal conductivity of granular media: a grain scale investigation, *Int. J. Therm. Sci.* 142 (2019) 266–279.
- [34] O. Birkholz, Y. Gan, M. Kamlah, Modeling the effective conductivity of the solid and the pore phase in granular materials using resistor networks, *Powder Technol.* 351 (2019) 54–65.
- [35] Q. Hou, Z. Zhou, A. Yu, Computational study of heat transfer in a bubbling fluidized bed with a horizontal tube, *AICHE J.* 58 (2012) 1422–1434.
- [36] Q. Hou, K. Dong, A. Yu, Dem study of the flow of cohesive particles in a screw feeder, *Powder Technol.* 256 (2014) 529–539.
- [37] J. Geng, E. Longhi, R. Behringer, D. Howell, Memory in two-dimensional heap experiments, *Phys. Rev. E* 64 (2001), 060301.
- [38] A. Vijayan, Y. Gan, R.K. Annabattula, Evolution of fabric in spherical granular assemblies under the influence of various loading conditions through dem, *Granul. Matter* 22 (2020) 1–15.
- [39] W. Fan, D. Gou, X. Liu, M. Li, X. An, K. Dong, R. Zou, H. Zhang, H. Fu, X. Yang, et al., Air impact induced densest amorphous granular materials: formation, dynamics, and mechanisms, *Phys. Rev. B* 105 (2022) L020202.
- [40] V. Richefeu, M.S. El Youssoufi, E. Azéma, F. Radjai, Force transmission in dry and wet granular media, *Powder Technol.* 190 (2009) 258–263.
- [41] F. Radjai, V. Richefeu, Bond anisotropy and cohesion of wet granular materials, *Philos. Trans. R. Soc. A Math. Phys. Eng. Sci.* 367 (2009) 5123–5138.
- [42] S. Luding, Anisotropy in cohesive, frictional granular media, *J. Phys. Condens. Matter* 17 (2005) S2623.
- [43] P.A. Cundall, O.D. Strack, A discrete numerical model for granular assemblies, *geotechnique* 29 (1979) 47–65.
- [44] O.R. Walton, Numerical simulation of inclined chute flows of monodisperse, inelastic, frictional spheres, *Mech. Mater.* 16 (1993) 239–247.
- [45] S. Luding, Cohesive, frictional powders: contact models for tension, *Granul. Matter* 10 (2008) 235.
- [46] C. Kloss, C. Goniva, A. Hager, S. Amberger, S. Pirker, Models, algorithms and validation for opensource dem and cfd-dem, *Prog. Comp. Fluid Dynam. Int. J.* 12 (2012) 140–152.
- [47] N.V. Brilliantov, F. Spahn, J.-M. Hertzsch, T. Pöschel, Model for collisions in granular gases, *Phys. Rev. E* 53 (1996) 5382.
- [48] K. Iwashita, M. Oda, Rolling resistance at contacts in simulation of shear band development by dem, *J. Eng. Mech.* 124 (1998) 285–292.
- [49] J. Ai, J.-F. Chen, J.M. Rotter, J.Y. Ooi, Assessment of rolling resistance models in discrete element simulations, *Powder Technol.* 206 (2011) 269–282.
- [50] R. Fuchs, T. Weinhart, J. Meyer, H. Zhuang, T. Staedler, X. Jiang, S. Luding, Rolling, sliding and torsion of micron-sized silica particles: experimental, numerical and theoretical analysis, *Granul. Matter* 16 (2014) 281–297.
- [51] H. Tang, R. Song, Y. Dong, X. Song, Measurement of restitution and friction coefficients for granular particles and discrete element simulation for the tests of glass beads, *Materials* 12 (2019) 3170.
- [52] A. Bhateja, I. Sharma, J.K. Singh, Scaling of granular temperature in vibro-fluidized grains, *Phys. Fluids* 28 (2016), 043301.
- [53] F. Soulie, F. Cherblanc, M.S. El Youssoufi, C. Saix, Influence of liquid bridges on the mechanical behaviour of polydisperse granular materials, *Int. J. Numer. Anal. Methods Geomech.* 30 (2006) 213–228.
- [54] C.D. Willett, M.J. Adams, S.A. Johnson, J.P. Seville, Capillary bridges between two spherical bodies, *Langmuir* 16 (2000) 9396–9405.
- [55] D. Kang, A. Nadim, M. Chugunova, Marangoni effects on a thin liquid film coating a sphere with axial or radial thermal gradients, *Phys. Fluids* 29 (2017), 072106.
- [56] G. Lian, C. Thornton, M.J. Adams, A theoretical study of the liquid bridge forces between two rigid spherical bodies, *J. Colloid Interface Sci.* 161 (1993) 138–147.
- [57] H. Chen, W. Liu, S. Li, Random loose packing of small particles with liquid cohesion, *AICHE J.* 65 (2019) 500–511.
- [58] A.-B. Huang, W.-J. Chang, H.-H. Hsu, Y.-J. Huang, A mist pluviation method for reconstituting silty sand specimens, *Eng. Geol.* 188 (2015) 1–9.
- [59] A. Tabaroei, S. Abrishami, E.S. Hosseiniinia, Comparison between two different pluviation setups of sand specimens, *J. Mater. Civ. Eng.* 29 (2017) 04017157.
- [60] M. Dong, J. Reimann, R.K. Annabattula, Y. Gan, Morphological characterisation of 2d packing with bi-disperse particles, *Int. J. Adv. Eng. Sci. Appl. Math.* 13 (2021) 89–97.
- [61] A.W. Bowman, A. Azzalini, *Applied Smoothing Techniques for Data Analysis: The Kernel Approach with S-Plus Illustrations* vol. 18, OUP Oxford, 1997.
- [62] J.-F. Ferellec, G.R. McDowell, A method to model realistic particle shape and inertia in dem, *Granul. Matter* 12 (2010) 459–467.
- [63] Y. Yuan, Y. Jiao, Y. Wang, S. Li, Universality of jammed frictional packing, *Phys. Rev. Res.* 3 (2021), 033084.
- [64] H.S. Katz, J.V. Milewski, *Handbook of Fillers and Reinforcements for Plastics*, Van Nostrand Reinhold Co, 1978.
- [65] S.S. Nadukuru, R.L. Michalowski, Arching in distribution of active load on retaining walls, *J. Geotech. Geoenviron.* 138 (2012) 575–584.